Ultrasonics 156 (2025) 107759

Contents lists available at ScienceDirect

Ultrasonics

journal homepage: www.elsevier.com/locate/ultras

Coherent Plane Wave Compounding combined with Euclidean distance transform for high frame rate and high contrast ultrafast imaging

Sajjad Afrakhteh *, Libertario Demi

Department of Information Engineering and Computer Science, University of Trento, Italy

ARTICLE INFO

Keywords:
Artifacts
CPWC
Contrast
Distance transform
Frame rate
Ultrafast
Ultrasound

ABSTRACT

Ultrasound Coherent Plane Wave Compounding (CPWC) is a beamforming technique that generally provides higher image contrast compared to single-angle plane wave imaging (PWI). However, when a reduced number of compounding angles is used to achieve higher frame rates, the contrast may degrade due to artifacts such as grating lobes, sidelobes, and ghost artifacts. In this study, our objective is to improve the image contrast in CPWC imaging while using a lower number of transmissions, reaching a higher frame rate and high contrast CPWC image. To this end, we propose a spatially weighted CPWC imaging based on the distance transform. More specifically, we propose utilizing the angle-wise Euclidean distance transform (EDT)- based filter as a joint post-beamformer to reduce the negative impact of grating lobes and ghosting artifacts in image contrast before coherently compounding the radio frequency (RF) images of different angles. By employing the proposed EDT-based technique, we do emphasize ‘on-axis’ information while suppressing ‘off-axis’ information, thereby reducing sidelobes, grating lobes, and ghosting artifacts. We applied the suggested technique to the plane wave imaging challenge in medical ultrasound (PICMUS) database, and the results revealed a significant improvement in image contrast while reaching a 5x improvement in the acquisition frame rate. Quantitative analysis of the proposed method using the generalized contrast-to-noise ratio (gCNR) across varying noise levels demonstrates its robustness in preserving cyst detectability. More specifically, the gCNR of the proposed technique remains consistently high, above 0.88, as SNR decreases from +9 dB to −21 dB, while CPWC shows a significant performance drop, with gCNR values dropping from 0.89 to 0.37. These results confirm that the proposed approach effectively maintains cyst detectability even under severe noise conditions.

1. Introduction

Ultrasound imaging is a pivotal medical diagnostic tool that enables visualization of internal organs. Its safety, owing to the absence of ionizing radiation, along with its real-time capabilities, portability, cost-effectiveness, and versatility, render it indispensable in modern medical diagnostics and monitoring [1].

Balancing parameters such as frame rate and image quality (resolution, and contrast) poses a significant challenge in ultrasound imaging. In conventional line-by-line ultrasound imaging, sequential beamforming is employed, where each frame is constructed by sequentially beamforming all the scan lines. This process requires separate transmissions for beamforming each scan line, which provides relatively acceptable spatial resolution, particularly with adaptive beamformers [2–6], but limits the frame rate to the number of scan lines in the image.

Several parallel beamforming approaches have been developed to enhance the frame rate of linear imaging by reducing the number of transmissions. One such approach is multi-line acquisition (MLA) [7], which involves parallelization in reception by beamforming multiple adjacent lines simultaneously for each transmission. Although MLA facilitates a higher frame rate, it comes with limitations such as decreased spatial resolution and penetration depth due to the broader transmission beam. In contrast to MLA, multi-line transmission (MLT) [8] employs multiple focused beams transmitted simultaneously in various directions, thereby improving the frame rate accordingly. However, MLT is susceptible to cross-talk artifacts arising from the simultaneous transmission of multiple beams. In addition, utilizing random or regular sampling, we proposed reconstruction techniques utilizing discrete cosine transform (DCT) [5], tensor completion [9], and radial basis functions (RBFs) [10] to reduce the trade-off between image quality and frame rate in linear focused imaging. Nevertheless, certain applications require frame rates in the kilohertz (kHz) range, such as ultrasound localization microscopy (ULM) [11], shear wave elastography (SWE) [12], and color Doppler imaging [13], which surpass the

* Corresponding author.
E-mail address: sajjad.afrakhteh@unitn.it (S. Afrakhteh).

https://doi.org/10.1016/j.ultras.2025.107759
Received 3 January 2025; Received in revised form 12 June 2025; Accepted 8 July 2025
Available online 21 July 2025

capabilities of focused ultrasound. To address the limitation of frame rate, plane wave imaging (PWI) was introduced [14], allowing for the beamforming of the entire image frame with a single transmission. While PWI achieves kHz frame rates, it comes at the cost of degraded image quality due to unfocused transmission.

To address the image quality issue in PWI, Montaldo et al. [15] proposed the coherent plane-wave compounding (CPWC) imaging strategy. CPWC involves performing PWI at different angles and then coherently combining the resulting images to achieve high-contrast images. However, increasing the number of transmissions in CPWC reduces the frame rate, necessitating a trade-off between image contrast and frame rate. Efforts have been made in the state of the art to mitigate the trade-off between image contrast and frame rate. Afrakhteh et al. in [16,17] proposed tensor completion- and RBF-based reconstruction techniques coupled with sparse transmission, employing random and regular transmission coding patterns, respectively. Although their approach enhanced the frame rate by 3 to 4 times, the selected coding patterns were suboptimal. Hashemseresht et al. [18] suggested minimum variance (MV)-based weighting before compounding to enhance image resolution. They also used coherence factor (CF) filtering to mitigate image artifacts with a reduced number of transmissions, consequently improving image contrast [18]. CF-based approaches have been proposed to enhance the image quality of CPWC images [19,20]. In [19], CF is defined as the ratio of the energy from the coherent sum to the total incoherent energy of the signals received across an aperture. This concept relies on the principle that, once focusing delays are applied, signals along the main axis (main lobe) exhibit strong coherence, while signals from the side lobes (off-axis) remain incoherent. The authors in [20] proposed the generalized coherence factor to extend CF idea into the spatial frequency domain. Unlike the standard CF, GCF adjusts the coherent energy calculation by incorporating not just the DC component but also low-frequency components from the spectrum of the aperture data. The other CF-based techniques include dynamic coherence factor (DCF) [21], zero-crossing coherence factor (ZCF) [22], and sign coherence factor (SCF) [23], aim to decrease noise levels and enhance contrast while accepting some compromise on the speckle pattern. Moreover, the Filtered Delay Multiply and Sum (F-DMAS) beamforming technique has been introduced as a non-linear beamformer that multiplies delayed signals before summation [24,25]. F-DMAS effectively exploits higher-order signal correlations, leading to improved image contrast, resolution, and superior clutter suppression compared to the traditional Delay-and-Sum (DAS) method. However, a notable limitation of F-DMAS is its increased computational complexity, which can lead to higher computational time. Short-Lag Spatial Coherence (SLSC) beamforming has also been proposed to address limitations of traditional intensity-based methods [26,27]. More specifically, instead of relying solely on signal amplitude, SLSC analyzes the spatial coherence of received echoes at small lag distances to beamform images. This coherence-based strategy enhances robustness to noise, clutter, and aberrations. Nevertheless, one limitation of SLSC is its tendency to reduce spatial resolution, as coherence measurements may smooth out fine structural details in the resulting images. Furthermore, deep learning (DL)-based techniques have been introduced in the literature [28–30], showing promising outcomes in the reconstruction of CPWC images. However, employing these techniques in real-time applications requires robust processing units and substantial amounts of training data to achieve high performance and generalizability.

It has been demonstrated in the state of the art that clutter noise sources such as grating lobes, side lobes, and axial lobes can affect the image contrast in CPWC images [31,32]. Among these sources, axial lobes are particularly significant in coherent compounding methods like CPWC. To address this issue, Rodriguez-Molares et al. [33] developed a theory explaining the mechanism behind axial lobe formation. Their theory suggests that applying a specific angle-dependent transmit apodization (ADTA) can eliminate axial lobes at the expense of reducing the field of view. Differentially, in this paper, we propose a novel approach using distance transform to mitigate imaging artifacts caused by sidelobes, grating lobes, and ghost artifacts, which contribute to lower contrast in CPWC imaging. It should be noted that ghost artifacts are axial lobes located below the point spread function that are caused by the spatial quantization of the aperture, which introduces a tail in the wavefront of the plane wave. More specifically, the proposed technique seeks to separate the main lobe 'on-axis' signal from the noise sources (off-axis signals) by leveraging the distance transform theory. Our method aims to improve CPWC's image contrast by reducing the level of these artifacts without compromising the field of view, which is an issue in ADTA. We will apply the technique to simulated, experimental, and *in vivo* datasets in the Plane-wave Imaging Challenge in the Medical UltraSound (PICMUS) database. The efficiency of the proposed technique in enhancing image contrast while maintaining or improving the acquisition frame rate by utilizing fewer transmissions will be evaluated.

2. Methods

2.1. Euclidean distance transform

The Euclidean Distance Transform (EDT) is a fundamental operation in image processing and computer vision [34]. It converts a binary image into a distance map, where each pixel's value represents its distance to the nearest feature pixel (i.e., pixel with an intensity value above a certain threshold). Feature pixels are often boundary or edge pixels, represented by '1' in a binary image, while background pixels are represented by '0'.

The Euclidean distance (d) between two points (x_1, z_1) and (x_2, z_2) in a 2D plane is given by:

$$d[(x_1, z_1), (x_2, z_2)] = \sqrt{a_x[(x_2 - x_1)]^2 + a_z[(z_2 - z_1)]^2}, \tag{1}$$

where $[a_x, a_z]$ represents the aspect ratio.

The goal of the EDT is to compute, for each pixel $p \in P$ in the binary image, the distance to the nearest feature pixel q. Mathematically, the Euclidean Distance Transform $D(p)$ is defined as:

$$D(p) = \min_{q \in Q} d(p, q), \tag{2}$$

where Q is the set of all feature pixels in the image while P represents the set of pixels for which the Euclidean distance to the nearest feature should be calculated.

To efficiently compute the EDT, we use an algorithm used in [35]. The computational complexity of the approach is in the order of $O(N_{pix})$, where N_{pix} is the total number of pixels in a 2D image. This method significantly reduces computational complexity compared to the naive approach [36], which would require checking the distance from each pixel to every feature pixel. This algorithm efficiently computes the anisotropic distance transform by first scanning along the rows (z-scan) and then along the columns (x-scan), adjusting the distances according to the specified aspect ratios. The result is a distance transform matrix D that accounts for anisotropic scaling.

2.2. Proposed CPWC imaging using EDT

The idea of the paper is to use EDT as a joint beamformer to reduce imaging artifacts caused by grating lobes, side lobes, and ghost artifacts. The main hypothesis of employing the EDT for image filtering is that it can effectively convert an image into a distance map, where each pixel's value represents the shortest distance to a predefined set of feature points such as edges or specific regions of interest. This transformation allows for a robust representation of spatial relationships within the image, enabling enhanced analysis and processing. By providing a clear metric for the proximity of pixels to key features, the EDT can help in noise reduction by filtering out small, isolated noise elements, and emphasizing larger and more significant structures.

In CPWC imaging, we utilize the abovementioned advantage of EDT to design a spatial filter in the beamforming stage. By calculating the EDT, one can create weighting schemes that de-emphasize off-axis signals, which are primarily responsible for these artifacts. This is achieved through adaptive filtering, where it is dynamically adjusted based on the distance information, thereby suppressing artifacts during the summation of echoes. Therefore, the formulation of the proposed CPWC technique, which utilize the EDT as a joint beamformer to delay and sum (DAS) technique, lies in the following steps:

Step 1: Acquiring the raw plane wave data along K different angles. At this stage, we have $S_{N_s \times N_{el} \times K}$ as the recorded data, where N_s, N_{el}, and K respectively indicate the number of time samples (fast time), number of transducer array elements, and number of angles.

Step 2: Beamform the raw data for each angle using the delay and sum (DAS) technique.

$$I_k(x,z,t) = \sum_{i=1}^{N_{el}} S\left(x_i, t_k\left(x,z,x_i;\theta_k\right)\right), \tag{3}$$

where t is the total time delay that each plane wave propagates in the medium at beamforming grid (x,z) and return to the transducer element i that can be calculated as follows:

$$t_k\left(x,z,x_i;\theta_k\right) = \frac{d_1 + d_2}{c}, \tag{4}$$

where d_1 and d_2 represent the distance from the transducer element i to the imaging point (x,z) and d_2 is the distance from the imaging point (x,z) to transducer element at θ_k.

Step 3: Apply EDT to $I_k(x,z)$ to construct the filter corresponding to θ_k. To this end, first, we construct a binarized matrix based on the I_k^{norm} values and a threshold (α):

$$B_k\left(x_0,z_0\right) = \begin{cases} 1 & \left|I_k^{\text{norm}}\left(x_0,z_0\right)\right| \geq \alpha \\ 0 & \left|I_k^{\text{norm}}\left(x_0,z_0\right)\right| < \alpha, \end{cases} \tag{5}$$

where norm indicates the normalized value. To decouple the point spread function (PSF) from the background, the logical 'Not' operation is applied to the extracted $B_k(x_0,z_0)$. This operation allows the background and PSF points to function as the Q and P sets within the EDT framework, respectively. As a result, the EDT values near the center of the PSF become larger than those at the borders, effectively emphasizing on-axis signals while de-emphasizing off-axis signals.
Next, we extract the EDT map for the resulting Q and P sets, followed by the normalization defined in Eq. (6). The resulting EDT map ($D_k(x,y)$) serves as the filtering function ($A_k(x,y)$) for the beamforming the image of kth angle ($k = 0,1,2,\dots,K$):

$$A_k(x,z) = D_{k_{\text{norm}}}(x,z) = \frac{D_k(x,z) - D_{k_{\min}}}{D_{k_{\max}} - D_{k_{\min}}}, \tag{6}$$

where $D_{k_{\min}}$ and $D_{k_{\max}}$ respectively indicate the minimum and maximum value of the EDT map corresponding to kth angle.

Step 4: Apply the EDT filter and compounding to achieve the final beamformed CPWC image:

$$I_{CPWC}(x,z) = \frac{1}{K}\sum_{k=1}^{K} A_k(x,z) I_k(x,z). \tag{7}$$

The whole process of the proposed pipeline is summarized in Fig. 1.

It is important to identify the optimal value of α parameter to achieve the best point spread function (PSF) in terms of spatial resolution. In this study, we choose the value to obtain the best spatial resolution. More specifically, the optimal α value can be determined based on resolution, which is measurable by the full width at half maximum (FWHM):

$$\alpha_{opt} = \arg\max_{\alpha}(\text{Resolution}_\alpha) = \arg\min_{\alpha}(\text{FWHM}_\alpha). \tag{8}$$

2.3. Evaluation metrics

To assess the image quality of the CPWC images obtained, we evaluate resolution and contrast using standard metrics. For resolution measurement, we employ the FWHM at a dynamic range of −6 dB. For contrast assessment, we utilize the contrast ratio (CR) and the contrast-to-noise ratio (CNR):

$$\text{CR(dB)} = 20\log_{10}\left(\frac{\mu_f}{\mu_b}\right), \tag{9}$$

$$\text{CNR(dB)} = 20\log_{10}\left(\frac{|\mu_f - \mu_b|}{\sqrt{(\sigma_b^2 + \sigma_f^2)/2}}\right), \tag{10}$$

where symbols μ_f and μ_b refer to the average intensity values within the foreground and background regions of interest (ROIs), respectively. Likewise, σ_f and σ_b denote the standard deviations of intensity values in these respective regions.

However, the CNR is dynamic range dependent. Unlike the CNR, the generalized CNR (gCNR) is robust to variations in dynamic range [37–40]. It is defined as:

$$\text{gCNR} = 1 - \int \min\{p_i(x), p_o(x)\}\,dx \tag{11}$$

where $p_i(x)$ and $p_o(x)$ represent the probability density functions (pdf) of the intensity of the cyst target and the background, respectively. The gCNR measures the ability to detect a cyst as an ideal observer.

Moreover, to evaluate the image quality w.r.t. speckle pattern, we use the speckle signal-to-noise ratio (sSNR) as follows:

$$\text{sSNR} = \frac{\mu_b}{\sigma_b}. \tag{12}$$

The ROIs for the calculation of the resolution and contrast parameters are shown in Fig. 2.

2.4. Comparative study

To provide a fair and comprehensive analysis, we compare the proposed technique with three important state-of-the-art noise reduction and contrast enhancement techniques: the coherence factor (CF) and generalized CF (GCF) beamformers (i.e., coherence-based techniques) [19,20], and F-DMAS. We conduct the comparison using three datasets from PICMUS, including simulated cyst targets, experimental cyst targets, and *in vivo* carotid data.

2.5. Dataset

To evaluate the performance of the proposed technique, similar to other works in the ultrasound community, we use the PICMUS database [41]. The database consists of simulated, experimental, and in vivo datasets for resolution and contrast evaluation. We evaluate the proposed method using these datasets, and compare its effectiveness to the original CPWC imaging with a different number of transmissions (i.e., 1PW, 7PW, 11PW, 15PW, and 75PW). It is important to note that evenly spaced angular sampling was used to simulate the limited number of transmissions (<75PW). These findings help to explore the potential to improve the trade-off between image quality and acquisition frame rate in CPWC imaging.

The simulation datasets were generated using Field II software [42, 43]. For all the PICMUS datasets, A 128-element linear array probe with a pitch of 300 μm and a transmission frequency of 5.208 MHz was employed. The PICMUS database includes 75 plane waves (PWs) within an angle range of −16° to +16°, with an angle spacing of 0.43°. The

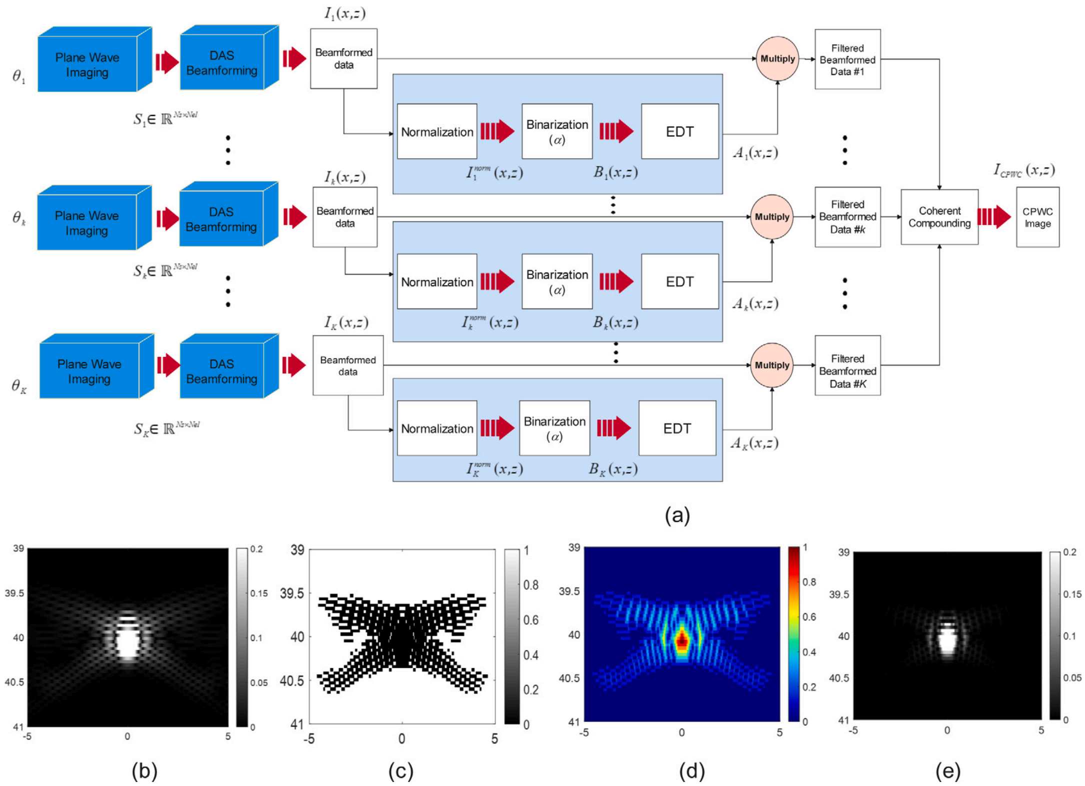

Fig. 1. (a) The block diagram of the suggested technique utilizing the EDT. It should be noted that $I_k(x, y)$ is the beamformed data that is envelope detected but not log-compressed before normalization. The figure also includes an example of the filtering process as (b) normalized beamformed DAS image, (c) binarized image. In the binary image, the points with binary values of '0' and '1' serve as P and Q sets in the EDT transform. (d) EDT weights, $A_k(x, y)$, and (e) EDT-filtered normalized beamformed DAS image.

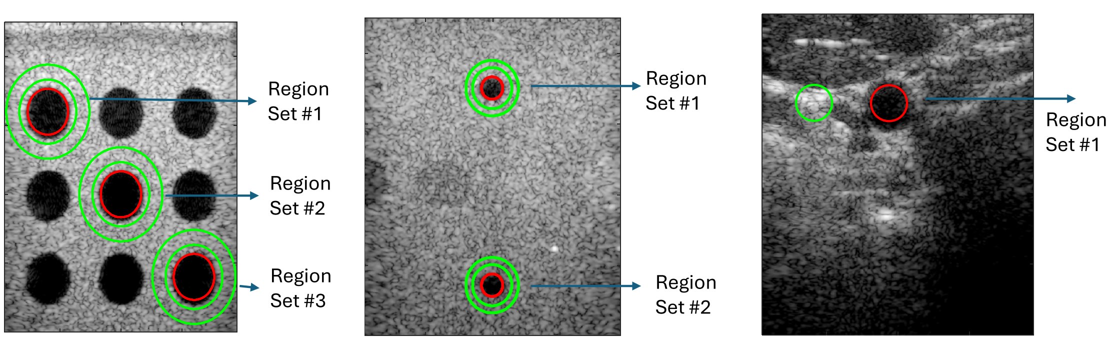

Fig. 2. Regions of interest (ROIs) used for contrast evaluation. The red and green colors respectively indicate the foreground and background areas. The first, second, and third columns show the regions for simulated cyst targets, experimental cyst targets, and *in vivo* carotid datasets from the PICMUS database, respectively.

f_{number} is also set to 1.75. The sampling frequency was set to four times the probe's center frequency ($f_s = 4f_c = 20.832$ MHz). In addition, the sound speed of 1540 m/s was assumed for the simulation.

However, before applying our method to the PICMUS database, we simulated a point spread function (PSF) at a depth of 40 mm to identify the optimal value of α parameter in EDT algorithm. The simulation pipeline was conducted using the Ultrasound Toolbox (USTB) [40]. More specifically, the optimal α value can be determined based on the PSF's lateral resolution, which is measurable by its FWHM as described in Eq. (8). We then implemented CPWC imaging with 15 angles spanning from $-16°$ to $+16°$. Our proposed beamforming technique utilized DAS combined with angle-wise EDT-based filtering, varying the α value from 10^{-4} to 10^{-2} in steps of 5×10^{-5} (200 different α values). It is important to note that we maintained the same acquisition settings and probe specifications in our PSF simulation as those used in the PICMUS database to ensure consistency throughout the paper. After calculating the α value, we apply the proposed technique to the PICMUS database.

3. Results

In the following, we provide the results of the evaluation of our proposed technique through different scenarios, including simulated, experimental, and in vivo datasets.

3.1. Simulated PSF

First, we carried out a simulation to determine the optimal value of α for thresholding before binarization in the EDT approach. To this end, we utilized the lateral FWHM criteria to determine the optimal α (see Eq. (8)). Fig. 4 shows the beamformed images of the PSF located at an axial distance of 40 mm using the original CPWC [15PW] and the proposed technique. The purpose of the simulation was to analyze the impact of the selected α value on image resolution and artifact appearance. The best (second column) and worst results (third column) for the proposed technique are reported in Fig. 4. Additionally, a video of the simulation results is provided via a link.

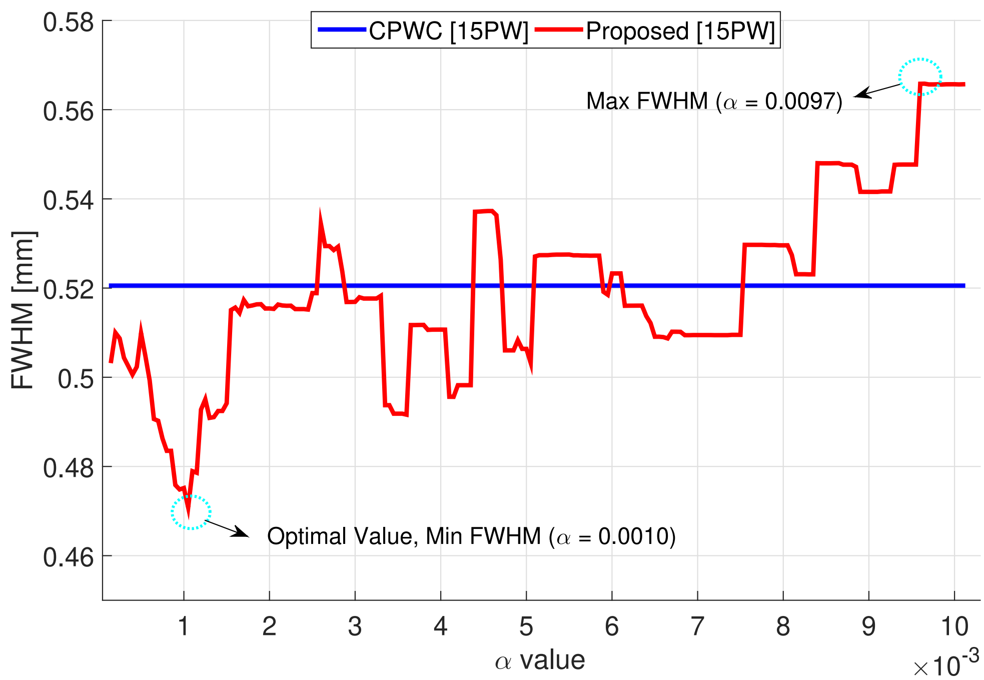

Fig. 3. Variation of the resolution w.r.t. changes in α values in the proposed EDT-based technique.

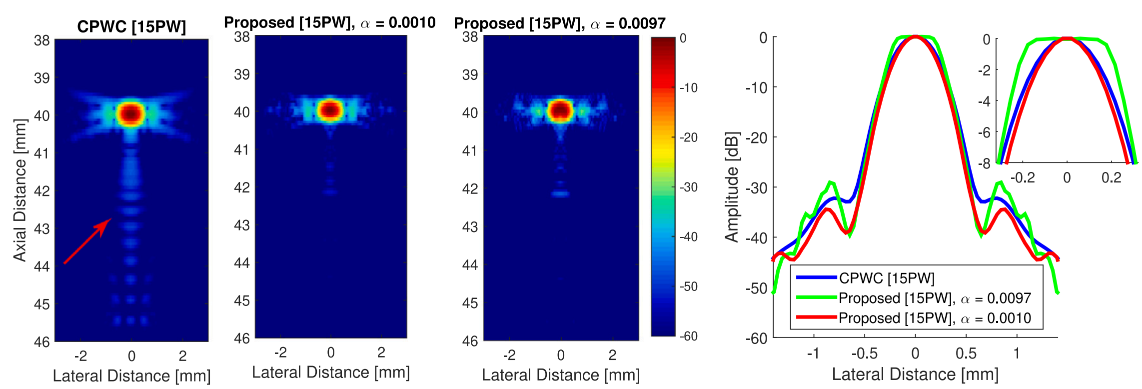

Fig. 4. Simulated point spread function (PSF) located at the lateral and axial coordinates of (0 mm,40 mm). The first column shows the beamformed image of PSF using the original CPWC image. The second and third columns show the beamformed images utilizing the proposed technique with the best (when using $\alpha = 0.0010$) and worst (when using $\alpha = 0.0097$) possible resolution. The results for all the analyzed values of α are provided in video format in the link. The red arrow in the first column indicates the artifacts in axial directions (i.e., ghost artifacts). PW: Plane Waves.

From the figure, it is evident that the original CPWC approach (first column) results in significant artifacts in both axial and lateral directions, degrading image quality and contrast. The application of the suggested EDT technique aims to reduce artifact levels, thereby improving image contrast. However, this improvement in image contrast may come at the cost of resolution degradation. Therefore, this study aims to select an optimal α value that minimizes the FWHM of the PSF. The variation of FWHM is summarized in Fig. 3. These simulation results demonstrated that our proposed technique successfully reduces artifact levels with the best resolution obtained at $\alpha = 0.001$. Therefore, based on the PSF resolution criteria, we applied the proposed technique with $\alpha = 0.001$ to other datasets from the PICMUS database.

3.2. Simulated point targets

Fig. 5 displays the beamformed images for both the proposed and original CPWC techniques for resolution assessment. We provided an example of A_k images used for the filtering at different angles for the case of 7PW in Fig. 6. The figure illustrates the spatially adaptive weighting maps $A_k(x,z)$ derived from the EDT for each of the seven transmission angles in the 7PW acquisition scenario. These angle-specific filters effectively emphasize on-axis regions—typically containing the main lobe energy—while progressively attenuating the off-axis regions that are more susceptible to grating lobes, sidelobes, and ghosting artifacts. As each beamformed image inherently differs in structure and focal geometry depending on its transmission angle, the EDT-derived filters adapt accordingly, centering the highest weights around the primary reflector locations. This selective weighting suppresses incoherent signal components that do not align with the main beam direction, which is particularly important when a reduced number of angles are used for compounding. The zoomed region at the depth of 35 mm reveals how the weight distribution responds to local image features. For each angle, the filter shows a bright, compact region with high weighting concentrated near the main lobe of the PSF, indicating strong coherence and signal strength. In contrast, the sidelobe parts exhibit a smooth and gradual attenuation in weighting, reflecting the suppression of spatially misaligned energy contributions. This results in improved image resolution after compounding the filtered beamformed data. The beamformed images clearly demonstrate that the proposed technique is highly effective in eliminating the imaging artifacts. This

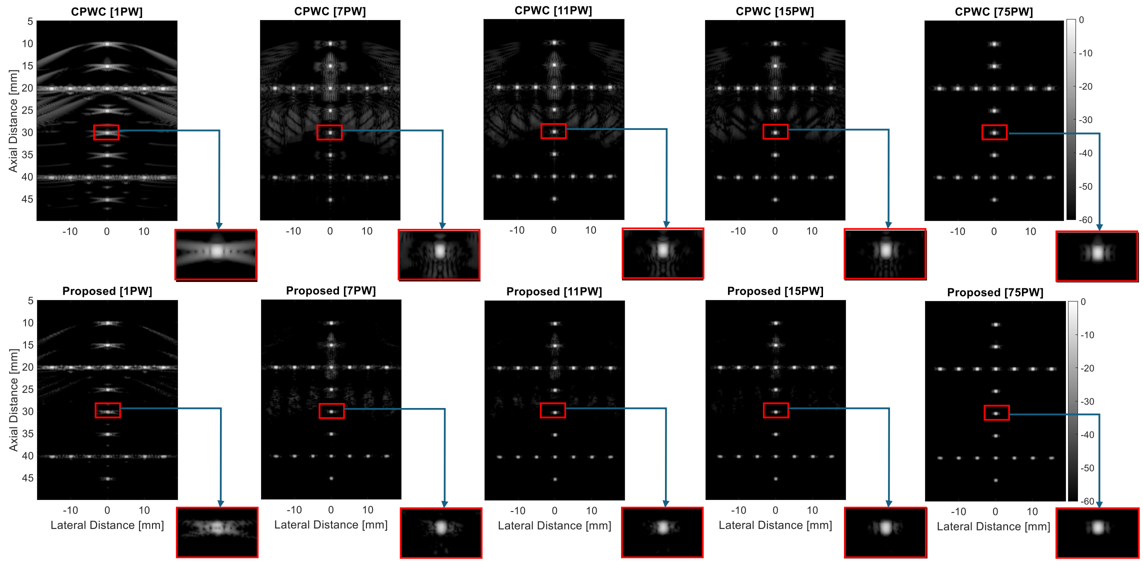

Fig. 5. The beamformed ultrasound images for the simulated point targets dataset in the PICMUS database using the original CPWC (first row) and the proposed technique (second row). The zoom of the PSF located at the depth of 30 mm is shown. The intensity values for the PSF located at depth of 45 mm is −14.6 dB, −14.7 dB, −14.8 dB, −14.5 dB, −14.3 dB for CPWC approach, while for the proposed technique are -18.2 dB, −18.1 dB,-17.8 dB,-17.6 dB,−17.4 dB. The values are presented for different number of PWs, 1,7,11,15,75,respectively.

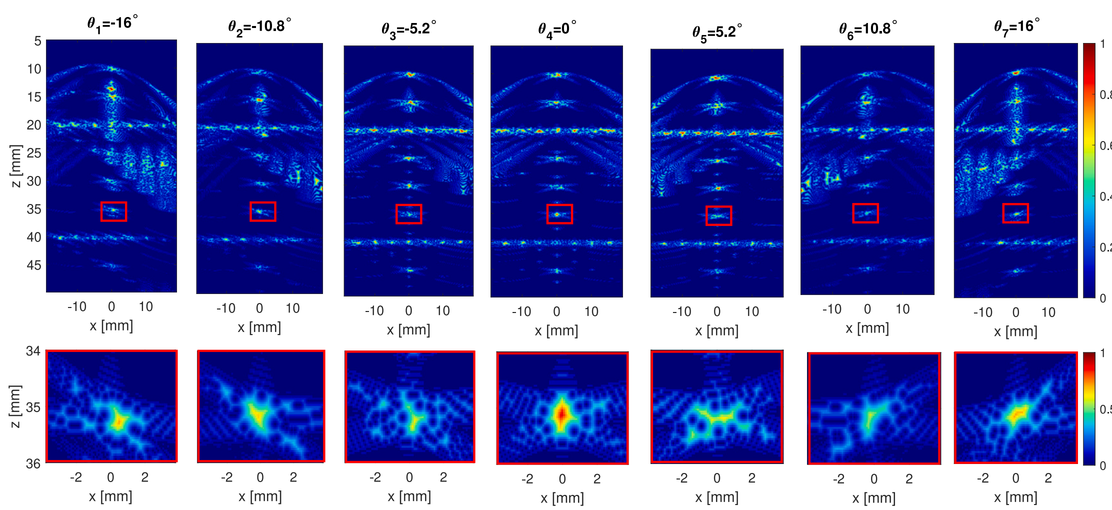

Fig. 6. An example of A_k filter for the different transmission angles involved in the 7PW case. The result is shown for the simulated point target dataset. The zoomed PSF at the depth of 35 mm is shown.

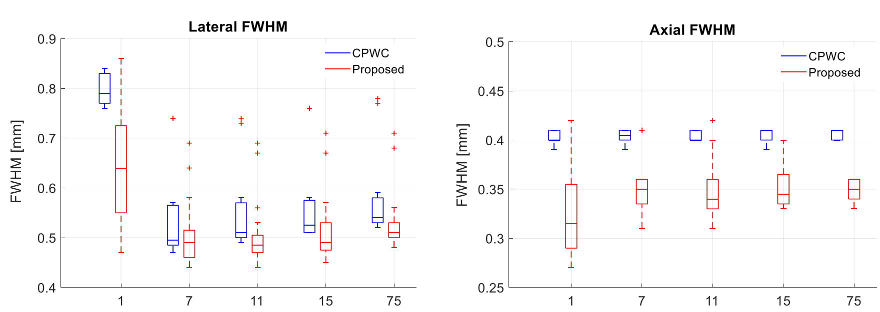

Fig. 7. Resolution evaluation (through lateral and axial FWHM) of the proposed technique compared to the original CPWC at different numbers of transmissions, i.e., 1, 7, 11, 15, and 75 PW. The results are shown as boxplots for all the point targets.

improvement allows us to reduce the number of transmissions from 75 to 15, achieving a 5x ($\frac{75}{15} = 5$) increase in the acquisition frame rate while maintaining image quality comparable to the original CPWC with 75 transmissions. It should be noted that at greater depths, the PSF resulting from a single plane wave (PW) exhibits reduced intensity, leading to lower weighting in both the EDT map and finally $A_k(x, z)$.

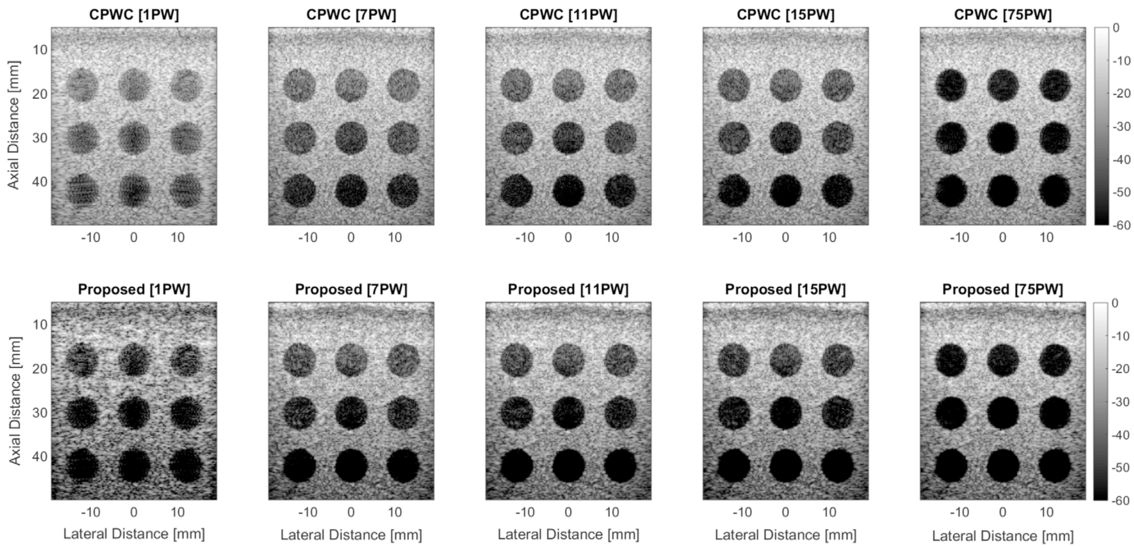

Fig. 8. The beamformed ultrasound images for the simulated cyst targets dataset in the PICMUS database using the original CPWC (first row) and the proposed technique (second row).

As a result, the PSF quality deteriorates with depth. However, this issue is mitigated when multiple angles are compounded, which enhances the PSF representation. Additionally, the resolution of simulated point targets was calculated in terms of −6 dB FWHM for all the point targets. We reported the lateral and axial FWHM values as boxplots in Fig. 7. It should be noted that the FWHM boxplots were derived from the resolution values of all 20 point targets, based on CPWC images generated using different numbers of transmissions (# Of Tx: 1, 7, 11, 15, and 75). In addition, the $\theta_k = 0$ is presented in all transmission sequences. The results indicated that our proposed technique not only maintains resolution but also enhances it, with the lateral FWHM values improving from 0.57 ± 0.08 mm to 0.52 ± 0.07 mm and axial values from 0.41 ± 0.01 mm to 0.35 ± 0.02 mm, while achieving a 5x improvement in acquisition frame rate. Thus, based on the resolution evaluation of the dataset, we can increase the acquisition frame rate by 5 times while also improving lateral and axial resolution compared to the CPWC with 75 transmissions.

3.3. Simulated cyst targets

For contrast evaluation, we first applied the proposed technique to the simulated cyst targets dataset, which includes nine circular cyst targets equally spaced in lateral and axial directions. The beamformed ultrasound images are shown in Fig. 8. Qualitatively, it is evident that applying the proposed technique significantly reduces artifacts. Specifically, by comparing the first and second rows of the figure at different number of transmission events, we can visually observe reduced artifact levels and sharpness, which help enhance image contrast. We quantified image contrast in terms of CR, CNR, sSNR, and gCNR for three cyst targets as shown in Fig. 2 and reported the parameters in Table 1, confirming promising improvement in CR and CNR parameters. Specifically, when aiming to increase the acquisition frame rate by a factor of five, the proposed technique achieves improvements of {CR, CNR} about {13.5 dB, 3.1 dB}, {11.3, 1.5 dB}, {7.8 dB, 1.7 dB} for cyst region sets 1,2, and 3 respectively. These enhancements are achieved while the sSNR is not compromised, highlighting the technique's effectiveness in enhancing background quality. The gCNR results indicate that the cysts in the data are easily detectable for both CPWC and the proposed technique, as both methods attain high gCNR scores (≥ 0.95), even when a lower number of PWs is used. The results also show that this improvement is not only achieved in comparison to CPWC at the same number of transmissions but is also comparable to or superior to CPWC with 75 transmissions.

3.4. Experimental cyst targets

Similarly, we applied the proposed technique to the experimental phantom containing two anechoic cysts within a fully speckled background (experimental cyst targets). The beamformed results are shown in Fig. 9. The experiment demonstrated the impact of our proposed technique in improving image contrast, as supported by the CR, CNR, and gCNR values in Table 2 for the three regions shown in Fig. 2. Specifically, when reducing the number of transmissions from 75 to 15 (achieving a fivefold improvement in acquisition frame rate), the improvements in {CR, CNR} were {6.1 dB, 1.2 dB} and {5.2 dB, 1.3 dB} for region sets 1 and 2, respectively. The improvements are achieved without significant compromise in sSNR. In this dataset, although the cysts in region sets #1 and #2 are easy to detect and even CPWC at lower number of PWs led to high gCNR scores, applying the proposed technique improved the gCNR scores for all the cases (# of PWs $\geq$ 7). Moreover, it can be observed that applying the proposed technique, at a reduced number of transmissions by a factor of 5, not only provided the comparable results to the case of using all 75 transmissions in original CPWC imaging, but also we can see improvement in CR, CNR, and gCNR.

3.5. In vivo carotid artery

To evaluate the applicability of the proposed technique for clinical applications, we applied it to *in vivo* carotid artery data. The beamformed results are shown in Fig. 10. Additionally, we included an example of A_k images for the case of 7 PWs in Fig. 11. The figure illustrates that the proposed filtering technique effectively mitigates noise and background interference, while enhancing the on-axis signals at various angles. This results in an improved image contrast and better texture visualization after compounding the filtered beamformed data. The beamformed images show a similar trend of improvement as observed with the simulated and experimental PICMUS datasets. Specifically, the proposed technique resulted in significant improvements in contrast parameters compared to the original CPWC. The beamformed images clearly show that the proposed technique provides a better depiction and separation of the carotid artery from the background. This analysis is supported by the contrast parameter values summarized in Table 3. As seen from the results, applying the proposed technique, while improving the frame rate by five times, leads to improvements in {CR, CNR} of {4.3 dB, 1.6 dB}. The gCNR results for the case of 15PW indicate that the proposed technique enhances detectability by

Table 1
The contrast parameters for the simulated cyst target data. The CR values are negative, the absolute values |CR| are reported for the parameter.

# of PWs	Methods	Region #1				Region #2				Region #3			
		|CR|	CNR	sSNR	gCNR	|CR|	CNR	sSNR	gCNR	|CR|	CNR	sSNR	gCNR
1	CPWC	16.3	9.0	2.4	0.87	21.8	10.7	3.3	0.92	18.3	9.9	4.2	0.90
	Proposed	23.8	8.5	2.5	0.84	31.8	10.4	3.1	0.90	26.4	9.7	4.0	0.87
7	CPWC	19.2	10.1	2.8	0.92	25.7	12.6	3.5	0.95	24.0	12.2	4.8	0.96
	Proposed	24.0	11.0	2.8	0.94	32.5	13.5	3.6	0.98	30.4	13.0	4.7	0.98
11	CPWC	21.8	11.4	2.6	0.95	29.4	13.7	3.4	0.98	26.9	13.2	4.6	0.97
	Proposed	26.6	12.8	2.6	0.97	35.8	14.9	3.5	0.99	33.8	14.5	4.7	0.99
15	CPWC	23.7	12.2	2.6	0.96	32.6	14.7	3.4	0.98	30.4	14.4	4.6	0.97
	Proposed	37.2	15.3	2.7	0.97	43.9	16.2	3.6	0.99	38.2	16.1	4.8	0.99
75	CPWC	39.4	15.5	2.6	0.98	44.6	16.1	3.3	0.98	36.7	15.2	4.4	0.98
	Proposed	42.0	15.9	2.7	1.00	49.2	16.6	3.5	1.00	44.5	15.5	4.7	0.99

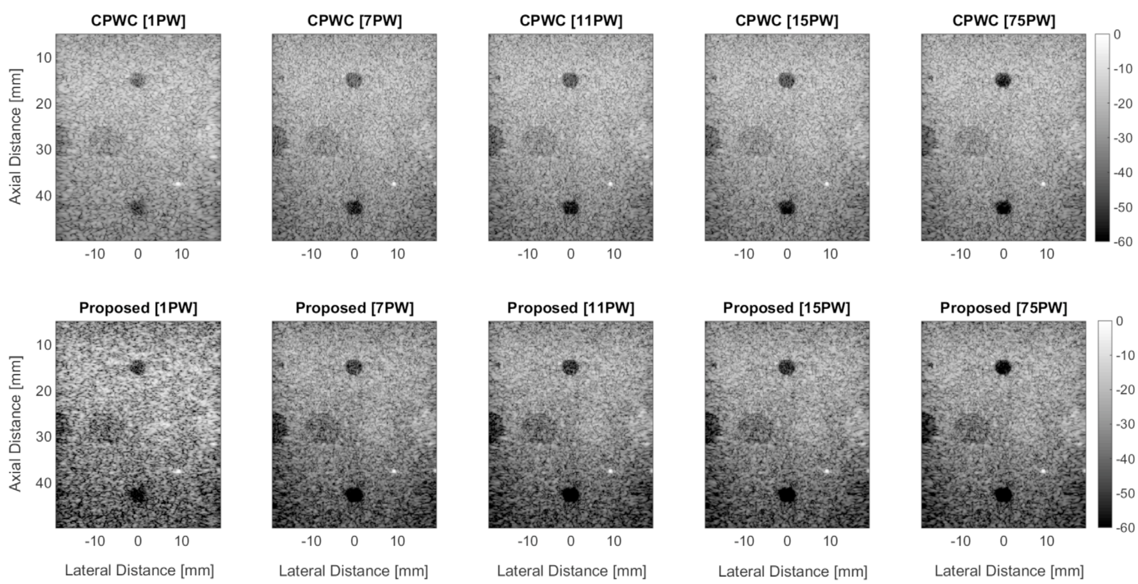

Fig. 9. The beamformed ultrasound images for the experimental cyst targets dataset in the PICMUS database using the original CPWC (first row) and the proposed technique (second row).

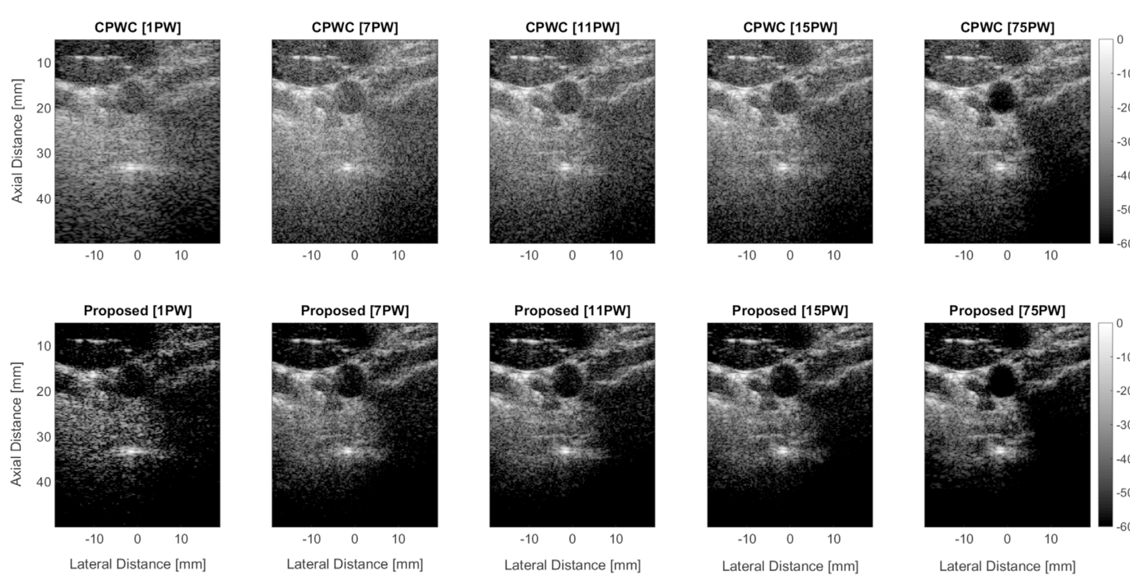

Fig. 10. The beamformed ultrasound images for the *in vivo* carotid dataset in the PICMUS database using the original CPWC (first row) and the proposed technique (second row).

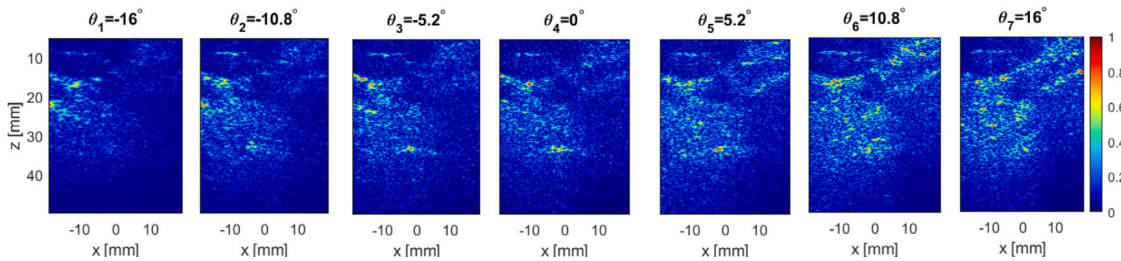

Fig. 11. An example of A_k filter for the different transmission angles involved in the 7PW case. The result is shown for the *in vivo* carotid dataset.

Table 2
Contrast parameters for the experimental cyst targets dataset.

# of PWs	Methods	Region #1				Region #2			
		CR	CNR	sSNR	gCNR	CR	CNR	sSNR	gCNR
1	CPWC	16.1	8.6	3.7	0.86	13.3	7.7	6.0	0.82
	Proposed	24.2	9.0	3.2	0.86	18.6	6.9	5.1	0.80
7	CPWC	18.4	10.2	4.0	0.90	19.3	10.5	6.5	0.91
	Proposed	22.6	11.1	4.3	0.93	24.4	11.6	6.9	0.92
11	CPWC	20.9	11.3	3.6	0.94	21.4	11.2	6.4	0.91
	Proposed	24.6	11.9	4.0	0.94	26.5	12.1	7.2	0.92
15	CPWC	21.8	11.6	3.7	0.93	22.0	11.5	6.3	0.92
	Proposed	25.7	12.6	3.9	0.96	27.2	12.2	7.1	0.94
75	CPWC	28.8	12.6	3.7	0.95	25.4	11.4	6.4	0.93
	Proposed	33.0	13.9	4.0	0.97	30.6	12.6	7.2	0.95

Table 3
Contrast parameters for the *in vivo* carotid artery data.

Method	Region # 1			
	CR	CNR	sSNR	gCNR
CPWC [1PW]	13.2	5.1	3.7	0.67
Proposed [1PW]	15.9	5.7	3.3	0.68
CPWC [7PW]	13.5	5.3	4.1	0.66
Proposed [7PW]	18.1	6.8	3.8	0.73
CPWC [11PW]	14.9	5.4	3.6	0.68
Proposed [11PW]	18.8	6.9	3.5	0.76
CPWC [15PW]	15.2	4.7	3.2	0.63
Proposed [15PW]	19.5	6.3	2.9	0.69
CPWC [75PW]	20.7	6.6	3.0	0.68
Proposed [75PW]	26.9	7.4	2.8	0.76

increasing the gCNR score from 0.64 to 0.69. Moreover, the contrast parameters achieved by the proposed technique at 15PW are comparable to those of the original CPWC at 75PW. Therefore, this experiment also demonstrates a consistent improvement in contrast parameters.

3.6. Cyst detectability analysis under varying noise levels

Given that the cyst regions in the PICMUS database reconstructed using the CPWC method already exhibit high gCNR values, the potential improvement in cyst detectability using the proposed technique may be limited. To better assess the performance of our method under more challenging conditions, we simulated two cysts located at depths of 20 mm and 40 mm. All parameter settings and configurations were kept consistent with the PICMUS database. After acquiring the RF data, we introduced Gaussian noise at various signal-to-noise ratio (SNR) levels ranging from −21 dB to +9 dB. Both the CPWC method and the proposed technique were then applied to obtain the final beamformed images. Fig. 12 displays the beamforming results using 15 uniformly spaced angles. Subsequently, we computed the gCNR values for the two cysts at each SNR levels based on the defined foreground and background regions. These results are illustrated in Fig. 13. As shown in the figure, the proposed method effectively enhances cyst detectability, even at low SNR values.

3.7. Comparison with other techniques

We also compared the proposed technique to CF and GCF, and F-DMAS beamformers which are important works in the state of the art for contrast enhancement in CPWC imaging. The results, at the same frame rate (i.e., 15 PWs), are shown in Fig. 14. As illustrated in the figure, coherence-based techniques significantly improve image contrast. However, this improvement comes with several drawbacks. First, the CF and GCF results show that the speckle pattern is degraded, leading to a granular structure in the background, likely due to over smoothing. This issue results in the disappearance of foreground structures with less brightness (e.g., the cyst region at a depth of 40 mm in the experimental phantom). In contrast, our proposed technique enhances image contrast while preserving the background textural structure. Secondly, applying coherence-based techniques results in the loss of important information at the edges and within tissue structures. This is evident in the carotid vessel and surrounding areas (indicated by red arrows). The structure of the tissue is significantly altered in both CF and GCF compared to the original CPWC, highlighting a major drawback of coherence-based techniques. However, for this dataset, our proposed technique efficiently improves image contrast while preserving all anatomical information. Finally, unlike the CF and GCF techniques, our proposed method results in less inhomogeneity in the background while increasing image depth. This comparison underscores the efficacy of our proposed technique in enhancing image contrast without compromising important image details or background texture. The F-DMAS beamforming results demonstrate an improved contrast compared to CPWC, particularly in terms of noise suppression and target clarity. When comparing F-DMAS with the proposed technique, the proposed method consistently delivers superior image quality. More specifically, both methods localize the cysts effectively, but the proposed method shows clearer boundaries and significantly reduced background noise, highlighting better contrast resolution. Moreover, the background speckle pattern is better preserved in all datasets. It should be noted that the F-DMAS improvement comes at the expense of huge computational complexity due to numerous number of multiplications.

3.8. Speckle quality assessment

The Kolmogorov–Smirnov (K-S) test is then conducted on predefined regions within the PICMUS challenge dataset. This statistical test is often used to assess whether the data conforms to a Rayleigh distribution. Regions that pass the K-S test at a significance level of 0.05 are identified as areas where speckle quality is preserved. We applied this test to both simulated and experimental cyst targets in the PICMUS database and calculated the fraction of regions that passed the K-S test. The results are shown in Fig. 15 as heatmaps for different number of PWs and varying the EDT's α value within the range of 10^{-5} to 10^{-3} by an increment of 4×10^{-5}.

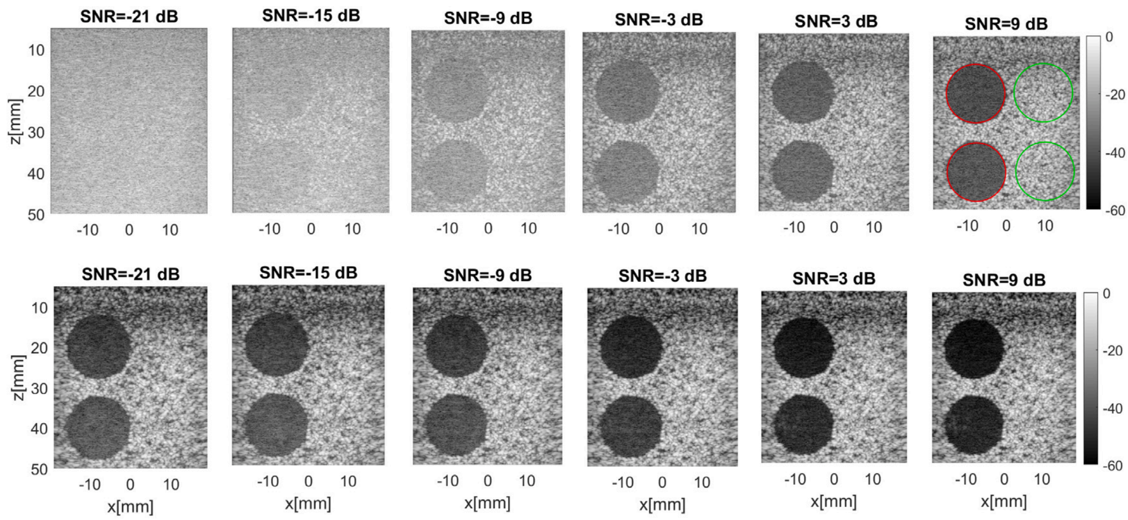

Fig. 12. Evaluation of the cyst detectability at different noise levels (i.e., different SNR levels). The first and second rows, respectively, show the beamformed images using CPWC and the proposed technique when using 15 angles. The red and green circles show the foreground and background regions for gCNR calculation, respectively.

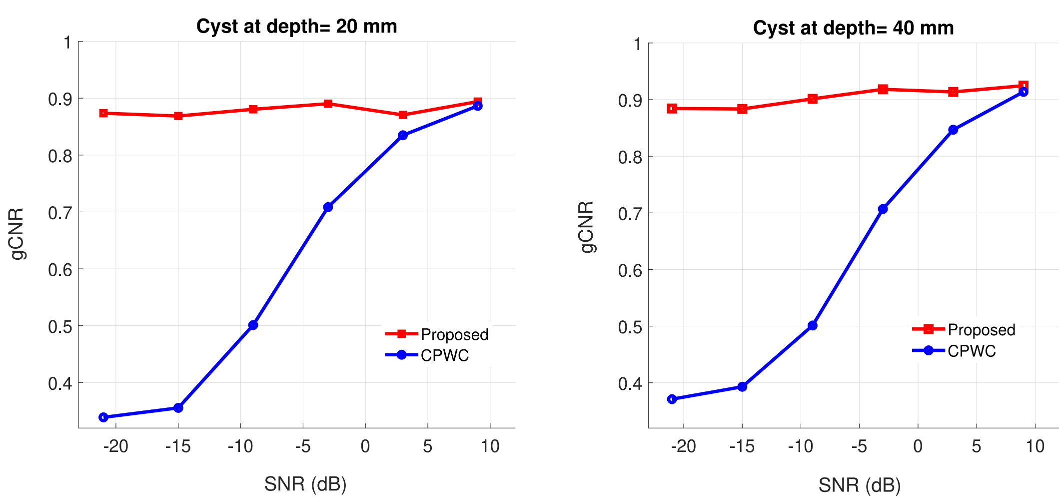

Fig. 13. Extracted gCNR values versus SNR for the cysts at different depths. The left and right columns show the results for the cysts located at depths of 20 mm and 40 mm, respectively.

3.9. Computational time

Finally, we report the computational time of the proposed technique in comparison to the original CPWC for all the datasets at different number of angles in Table 4. All software experiments were conducted using MATLAB software (MathWorks Inc., Natick, MA) on a 64-bit system with an Intel® CoreTM i7-8700K central processing unit (CPU) @ 3.70 GHz and 32 GB of random access memory (RAM).

Table 4
The computational time of the proposed technique (i.e., CPWC+EDT) compared with the original CPWC for different datasets and numbers of PWs. The values have the unit of Seconds.

Method	Simulated point targets	Simulated Cyst targets	Exprtimental Cyst targets	*In vivo* Carotid
CPWC [1PW]	3.79	5.02	8.68	3.70
Proposed [1PW]	3.84	5.09	8.79	3.76
CPWC [7PW]	16.55	20.51	40.21	18.57
Proposed [7PW]	16.75	20.68	40.58	18.74
CPWC [11PW]	25.02	30.40	56.01	27.39
Proposed [11PW]	25.26	30.62	56.42	27.62
CPWC [15PW]	35.43	40.73	74.83	34.29
Proposed [15PW]	35.72	41.04	75.50	34.55
CPWC [75PW]	163.86	197.25	399.08	172.51
Proposed [75PW]	165.12	198.69	401.79	173.79

4. Discussion and conclusion

Our study's findings demonstrated the significant improvements in ultrasound CPWC's imaging quality achieved through the proposed beamforming utilizing angle-wise EDT-based filtering. First, using a PSF simulation study, by identifying an optimal α value of 0.001, we ensured an effective balance between artifact reduction and resolution enhancement. This optimal value facilitated substantial improvements in image quality by minimizing ghost artifacts, sidelobe levels, and grating lobes, as shown in our −6 dB FWHM measurements. Nevertheless, at higher α values (e.g., $\alpha \geq 0.009$), we can see a plateau in the lateral profile. To justify, at higher α values the feature pixel set (Q set) expands, while the P set becomes more restricted. This results in a more uniform weight function surrounding the PSF, creating a plateau effect.

Following that, we applied the proposed technique to the PICMUS database. The CPWC's results of the simulated point targets showed that as the number of transmissions is lower, the negative impact of the clutter noise sources, especially axial lobes is more sensible. However, application of the proposed technique led to significant suppression of

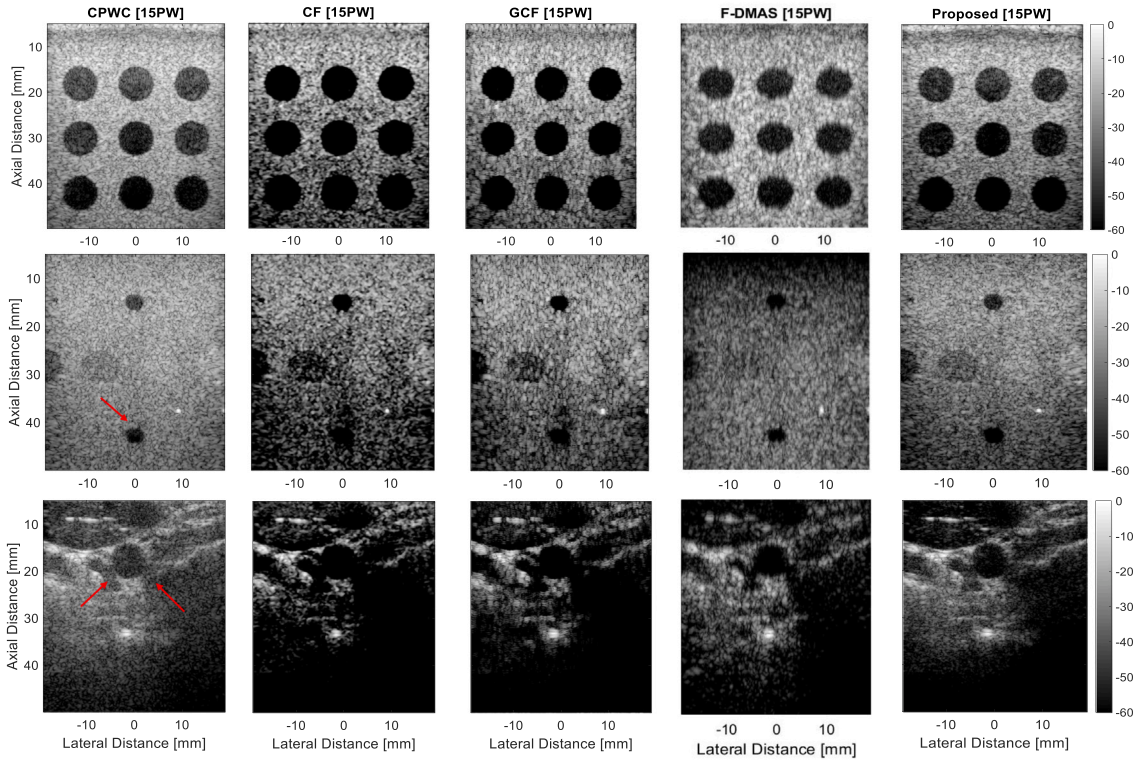

Fig. 14. Comparing the proposed technique with coherence factor (CF), generalized coherence factor (GCF), and F-DMAS techniques for contrast enhancement. The red arrows show the areas lost due to using the coherence-based techniques. The results are provided for 15 PWs which implies $5x$ acquisition frame rate enhancement.

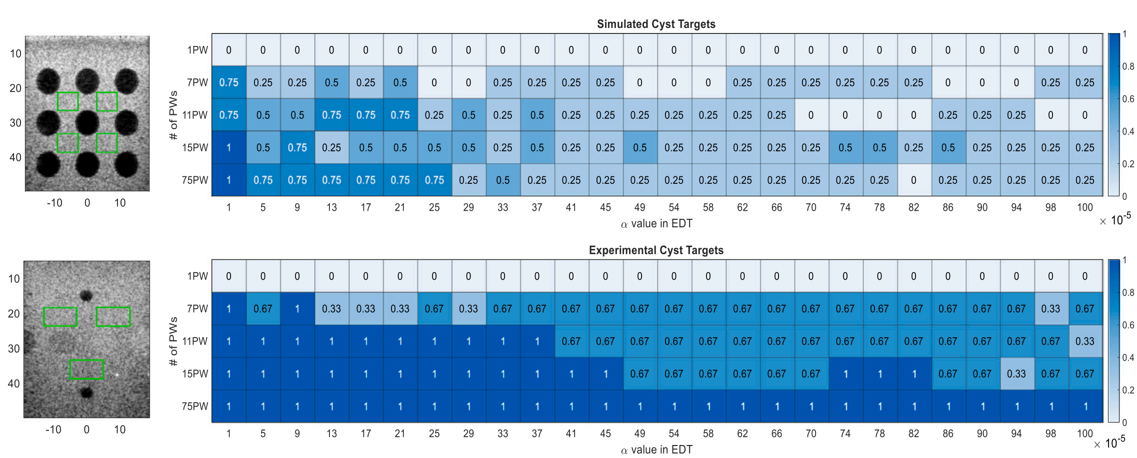

Fig. 15. The heatmaps represent the fraction of the areas in which the proposed technique passed the Kolmogorov–Smirnov (K-S) test. The evaluation areas for the test are shown in the first column (The same areas in the PICMUS challenge evaluation).

the axial lobes and side lobes. In addition, the FWHM results demonstrated that the proposed technique helped to improve the axial and lateral resolution even when using a single transmission.

Next, the evaluations on simulated cyst targets demonstrated significant improvement in contrast parameters. Additionally, we evaluated the potential for reducing the number of transmissions in CPWC imaging, thereby enhancing the frame rate while maintaining high image quality, effectively improving the trade-off between frame rate and image quality. The results indicated that we could improve the acquisition frame rate by a factor of 5 (using 15 equally spaced angular transmissions), with image quality either superior to or comparable to that of CPWC with 75 transmissions. The high gCNR scores observed in the data set show that even CPWC with a lower number of transmissions achieves high detectability of cyst targets. This indicates that the dataset may not be ideal for assessing improvements in gCNR, as it already exhibits strong detectability.

The practical applicability of our proposed technique was further validated through experimental and *in vivo* datasets. In these settings, our method consistently delivered superior image quality, significantly enhancing CR and CNR without a substantial trade-off in sSNR. Even when acquisition frame rates were increased, our technique maintained high image contrast, outperforming the original CPWC approach. In the experimental dataset, similar to the simulated cyst targets, gCNR measurements for region sets #1 and #2 indicate that cysts are easily detectable with a higher number of transmissions ($\geq$ 7) even when using the original CPWC approach. However, the proposed technique provides a slight improvement in gCNR, even at 15 PWs. The *in vivo* carotid gCNR analysis also demonstrated a promising improvement

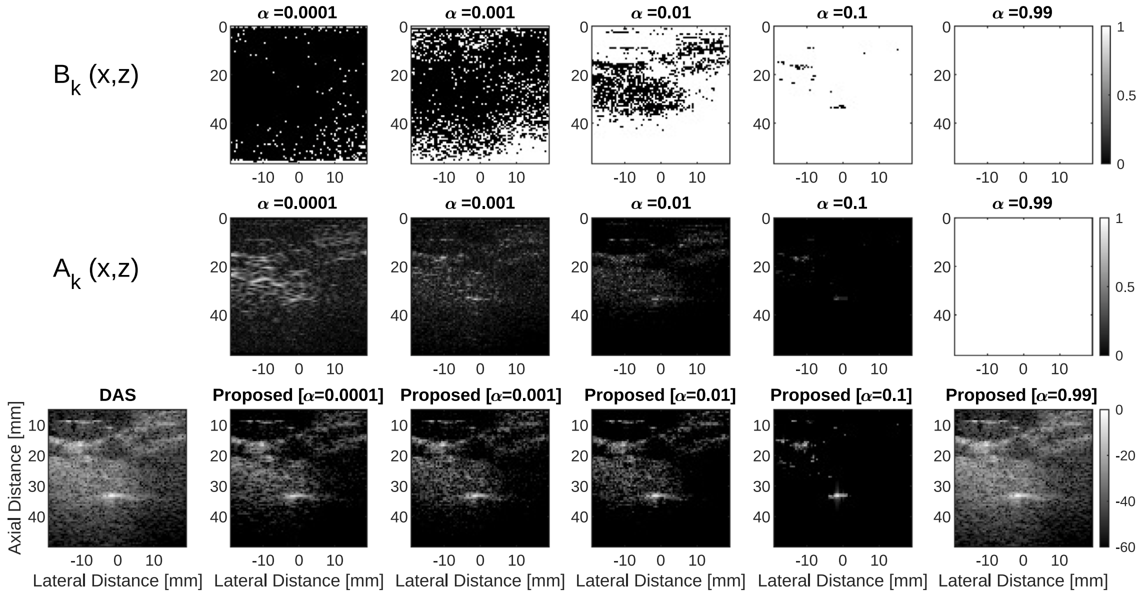

Fig. 16. Impact of α value on the size of P set and Q set in EDT Transform. For $\alpha > 0.99$, the results converge to DAS. This results are shown for a single plane wave with $\theta_k = 0$.

with the proposed technique, indicating that it effectively enhances not only CR and CNR, but also gCNR, without significant compromise in sSNR.

We comprehensively evaluated the cyst detectability under varying noise conditions for both CPWC and the proposed imaging technique. Fig. 12 shows beamformed images of two cysts located at different depths, across a range of SNR levels from −21 dB to +9 dB. The first row (CPWC results) reveals a marked degradation in image quality as the noise level increases, with the cysts becoming almost indistinguishable from the background at SNRs below −9 dB. In contrast, the second row demonstrates the robustness of the proposed technique, which consistently maintains cyst visibility even under severe noise conditions. This highlights the superior noise resilience and contrast preservation of the proposed method compared to CPWC. The quantitative analysis shown in Fig. 13 further supports these visual observations through the computation of gCNR values at depths of 20 mm and 40 mm. For both depths, the proposed method maintains a high gCNR (around 0.9) across all tested SNRs, indicating reliable cyst detectability irrespective of noise levels. In contrast, CPWC demonstrates a steep decline in gCNR under low SNR conditions, with significant improvements only becoming evident at SNRs above −3 dB.

Moreover, compared to coherence-based techniques such as CF and GCF, our method preserved structural background texture, avoiding oversmoothing issues that these techniques often introduce. This balance between contrast enhancement and structural preservation demonstrates the robustness of our approach, highlighting its clinical potential for various medical ultrasound imaging applications.

One question that may arise is the reason that $\alpha = 0.01$ is selected as the maximum value in our analysis. Fig. 16 shows an empirical analysis to address this question. The visual analysis presented in the figure underscores the impact of the binarization threshold parameter α on the construction of sets P and Q, which are critical to the EDT-based beamforming method. The top two rows illustrate how varying α affects the binary mask $B_k(x,z)$ and the resulting distance-transformed map $A_k(x,z)$. As α increases, the density of selected features in the Q set grows while the corresponding P set shrinks, resulting in minimal spatial differentiation at $\alpha = 0.99$. This leads to EDT maps that are increasingly sparse and uniform, as evidenced by the near-constant intensity across the field in both B_k and A_k. Such convergence reflects a degenerate scenario where the algorithm mimics the DAS output due to the dominance of the default background values assigned to Q. The bottom row, which shows the final beamformed images under various α configurations, confirms this convergence and highlights the trade-off inherent in choosing α. At very low α values (e.g., $\alpha \leq 0.001$), the images suffer from high levels of speckle and noise due to an overly expansive P set. As α increases toward the optimal value of 0.01, the images become clearer, with better contrast and delineation of structures, indicating a balanced contribution from both sets. However, further increases in α (e.g., $\alpha = 0.1$ or 0.99) introduce pronounced darkening and loss of structural information—a direct result of excessive smoothing from the diminished P set. These results validate the choice of $\alpha = 0.01$ as an effective typical maximum that still maintains spatial detail without introducing artifacts or degenerating into DAS outputs.

It is important to acknowledge that the proposed EDT-based method is sensitive to the attenuation of signal amplitude with increasing depth. Because deeper structures tend to have weaker signal strength, using a global threshold for binarization may fail to adequately capture these features in the EDT map. This results in a lower signal-to-noise ratio (SNR) in the deeper regions of the beamformed image. Applying time gain compensation (TGC) to the beamformed data can enhance the SNR. To evaluate this effect, we applied TGC to carotid data and measured the SNR before and after its application within a red-marked rectangular region at greater depths. The results, summarized in Fig. 17, show an improvement in SNR from 1.59 dB to 2.38 dB, demonstrating that TGC helps amplify deeper features. While TGC partially addresses depth-related attenuation, future research could investigate adaptive or depth-specific thresholding methods.

As shown, CPWC [75 PW] achieved the highest image quality in conventional CPWC imaging, albeit at the cost of a reduced acquisition frame rate. In contrast, our proposed method can reduce the number of required transmission angles to 15 without a notable loss in image quality. More specifically, given the maximum depth (d_{max}) of 50 mm in the PICMUS dataset, the maximum pulse repetition frequency (PRF) is calculated as $PRF_{max} = \frac{c}{2d_{max}} = \frac{1540}{2\times0.05} = 15.4$ kHz. Accordingly, the maximum acquisition frame rate for CPWC [75 PW] is $PRF_{max}/N_a = 15400/75 \approx 205$ Hz, while our method achieves a substantially higher frame rate of approximately 1025 Hz.

Table 4 provides a comparison of computational times (beamforming times) between the proposed method and the CPWC technique across various datasets and different numbers of plane waves. The results indicate that the proposed technique is efficient, as it does not introduce a significant increase in computational time. Of course, the efficiency varies depending on the dataset size and the number of plane waves used in each scenario.

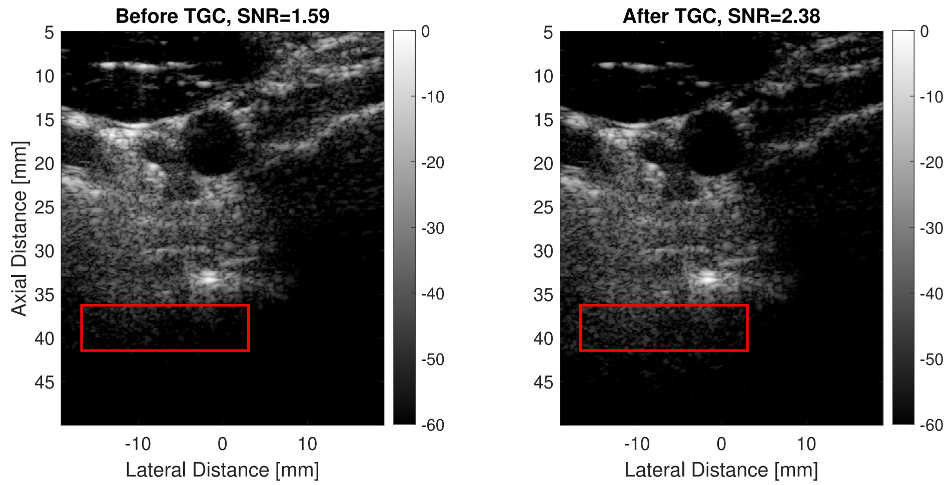

Fig. 17. An example of the impact of TGC on improving the SNR at deeper features of the EDT-based beamformed image. The red box shows the region for the SNR calculation.

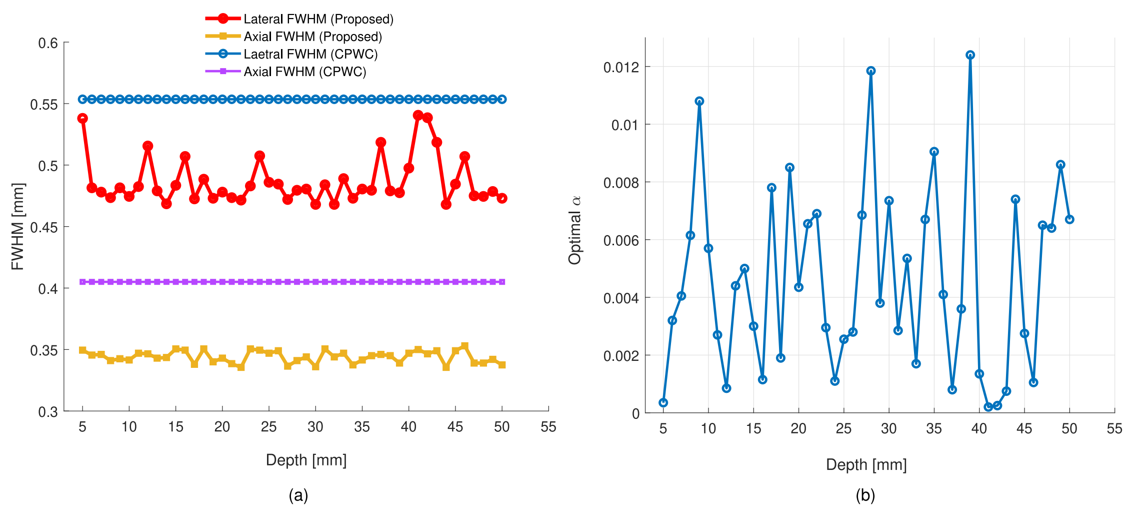

Fig. 18. (a) Variation of the lateral and axial resolution of the simulated point targets at different optimized depths. The average values across 20 point targets' FWHMs are reported for each depth. The results are shown for 15PW case. (b) Optimal α values extracted at each depth from 5 to 50 mm.

One of the limitation of the proposed technique, similar to other nonelinear beamformers, is its low capability in preserving the speckle pattern. The K-S test results in Fig. 15 for both simulated and experimental data show that the proposed technique is not able to pass the test under varying α values. However, the results show that the preservation of the speckle pattern can be improved by increasing the number of angles while compromising the frame rate.

Moreover, the robustness of this approach is influenced by the depth at which the α optimization is performed. To investigate this effect, we varied the depth of the PSF in Fig. 4 from 5 mm to 50 mm in 1 mm increments and extracted the optimal α values based on the lateral resolution at each depth. We then calculated the lateral and axial resolution of simulated point targets for each optimized depth. Fig. 18(a) displays the average FWHM values computed from 20 point targets at each depth for both the proposed method and CPWC. The proposed approach consistently yields improved lateral resolution while maintaining stable axial performance. Fig. 18(b) illustrates the corresponding optimal α values selected at each depth. While α generally varies smoothly within a low range, a more pronounced fluctuation is observed near 42 mm depth. This deviation is likely due to the small optimized α value. Specifically, a very small α value at this depth may have affected the binarization step. This result highlights the local sensitivity of the method to α in regions where structural transitions or low-contrast features occur, which is an open area for further tuning or robustness improvement.

However, in a future study, we plan to determine the value using the histogram of the global (i.e., whole image intensity statistical analysis) or local (i.e., window-based image intensity statistical analysis) analysis of the beamformed ultrasound RF data. By analyzing the histogram, we aim to adaptively select the α value based on the distribution characteristics of the RF data, potentially leading to a more robust and optimal performance of the technique across varying imaging conditions and types of data. This approach could help in better mitigating artifacts and improving overall image quality by tailoring the α value to the specific characteristics of each dataset.

CRediT authorship contribution statement

Sajjad Afrakhteh: Writing – review & editing, Writing – original draft, Visualization, Validation, Software, Methodology, Investigation, Formal analysis, Data curation, Conceptualization. **Libertario Demi:** Writing – review & editing, Visualization, Supervision, Funding acquisition.

Declaration of competing interest

The authors declare that they have no known competing financial interests or personal relationships that could have appeared to influence the work reported in this paper.

Data availability

Data will be made available on request.

References

[1] J.A. Jensen, Medical ultrasound imaging, Prog. Biophys. Mol. Biol. 93 (1) (2007) 153–165, http://dx.doi.org/10.1016/j.pbiomolbio.2006.07.025, URL https://www.sciencedirect.com/science/article/pii/S0079610706000861, Effects of ultrasound and infrasound relevant to human health.

[2] J.F. Synnevag, A. Austeng, S. Holm, Adaptive beamforming applied to medical ultrasound imaging, IEEE Trans. Ultrason. Ferroelectr. Freq. Control 54 (8) (2007) 1606–1613.

[3] S. Afrakhteh, H. Behnam, Low-complexity adaptive minimum variance ultrasound beam-former based on diagonalization, Biomed. Signal Process. Control. 62 (2020) 102110.

[4] B.M. Asl, A. Mahloojifar, A low-complexity adaptive beamformer for ultrasound imaging using structured covariance matrix, IEEE Trans. Ultrason. Ferroelectr. Freq. Control 59 (4) (2012) 660–667.

[5] S. Afrakhteh, H. Behnam, A fast and high frame rate adaptive beamforming using DCT-based RF-line recovery in line-by-line ultrasound imaging, Int. J. Imaging Syst. Technol. 30 (4) (2020) 1080–1094.

[6] B.M. Asl, A. Mahloojifar, Minimum variance beamforming combined with adaptive coherence weighting applied to medical ultrasound imaging, IEEE Trans. Ultrason. Ferroelectr. Freq. Control 56 (9) (2009) 1923–1931.

[7] D.P. Shattuck, M.D. Weinshenker, S.W. Smith, O.T. von Ramm, Explososcan: A parallel processing technique for high speed ultrasound imaging with linear phased arrays, J. Acoust. Soc. Am. 75 (4) (1984) 1273–1282.

[8] G. Matrone, A. Ramalli, A.S. Savoia, P. Tortoli, G. Magenes, High frame-rate, high resolution ultrasound imaging with multi-line transmission and filtered-delay multiply and sum beamforming, IEEE Trans. Med. Imaging 36 (2) (2016) 478–486.

[9] S. Afrakhteh, G. Iacca, L. Demi, High frame rate ultrasound imaging by means of tensor completion: Application to echocardiography, IEEE Trans. Ultrason. Ferroelectr. Freq. Control 70 (1) (2022) 41–51.

[10] H. Jalilian, S. Afrakhteh, G. Iacca, L. Demi, Increasing frame rate of echocardiography based on a novel 2d spatio-temporal meshless interpolation, Ultrasonics 131 (2023) 106953.

[11] G. Tuccio, S. Afrakhteh, G. Iacca, L. Demi, Time efficient ultrasound localization microscopy based on a novel radial basis function 2D interpolation, IEEE Trans. Med. Imaging (2023).

[12] P. Song, H. Zhao, A. Manduca, M.W. Urban, J.F. Greenleaf, S. Chen, Comb-push ultrasound shear elastography (CUSE): a novel method for two-dimensional shear elasticity imaging of soft tissues, IEEE Trans. Med. Imaging 31 (9) (2012) 1821–1832.

[13] M. Bruce, A. Hannah, R. Hammond, Z.Z. Khaing, C. Tremblay-Darveau, P.N. Burns, C.P. Hofstetter, High-frequency nonlinear doppler contrast-enhanced ultrasound imaging of blood flow, IEEE Trans. Ultrason. Ferroelectr. Freq. Control 67 (9) (2020) 1776–1784.

[14] M. Tanter, M. Fink, Ultrafast imaging in biomedical ultrasound, IEEE Trans. Ultrason. Ferroelectr. Freq. Control 61 (1) (2014) 102–119.

[15] G. Montaldo, M. Tanter, J. Bercoff, N. Benech, M. Fink, Coherent plane-wave compounding for very high frame rate ultrasonography and transient elastography, IEEE Trans. Ultrason. Ferroelectr. Freq. Control 56 (3) (2009) 489–506.

[16] S. Afrakhteh, H. Behnam, Coherent plane wave compounding combined with tensor completion applied for ultrafast imaging, IEEE Trans. Ultrason. Ferroelectr. Freq. Control 68 (10) (2021) 3094–3103.

[17] S. Afrakhteh, G. Iacca, L. Demi, A two-dimensional angular interpolation based on radial basis functions for high frame rate ultrafast imaging, J. Acoust. Soc. Am. 154 (5) (2023) 3454–3465.

[18] M. Hashemseresht, S. Afrakhteh, H. Behnam, High-resolution and high-contrast ultrafast ultrasound imaging using coherent plane wave adaptive compounding, Biomed. Signal Process. Control. 73 (2022) 103446.

[19] K. Hollman, K. Rigby, M. O'donnell, Coherence factor of speckle from a multi-row probe, in: 1999 IEEE Ultrasonics Symposium. Proceedings. International Symposium (Cat. No. 99CH37027), Vol. 2, IEEE, 1999, pp. 1257–1260.

[20] P.-C. Li, M.-L. Li, Adaptive imaging using the generalized coherence factor, IEEE Trans. Ultrason. Ferroelectr. Freq. Control 50 (2) (2003) 128–141.

[21] Y. Wang, C. Zheng, H. Peng, Dynamic coherence factor based on the standard deviation for coherent plane-wave compounding, Comput. Biol. Med. 108 (2019) 249–262.

[22] C. Zheng, H. Wang, X. Xu, H. Peng, Q. Chen, An adaptive imaging method for ultrasound coherent plane-wave compounding based on the subarray zero-cross factor, Ultrasonics 100 (2020) 105978.

[23] Y. Chen, Q. Kong, Z. Xiong, Q. Mao, M. Chen, C. Lu, Improved coherent plane-wave compounding using sign coherence factor weighting for frequency-domain beamforming, Ultrasound Med. Biol. 49 (3) (2023) 802–819.

[24] G. Matrone, A.S. Savoia, G. Magenes, Filtered delay multiply and sum beamforming in plane-wave ultrasound imaging: Tests on simulated and experimental data, in: 2016 IEEE International Ultrasonics Symposium, IUS, IEEE, 2016, pp. 1–4.

[25] F. Prieur, O.M.H. Rindal, A. Austeng, Signal coherence and image amplitude with the filtered delay multiply and sum beamformer, IEEE Trans. Ultrason. Ferroelectr. Freq. Control 65 (7) (2018) 1133–1140.

[26] Y. Wang, C. Zheng, H. Peng, C. Zhang, Coherent plane-wave compounding based on normalized autocorrelation factor, IEEE Access 6 (2018) 36927–36938.

[27] M.A. Lediju, G.E. Trahey, B.C. Byram, J.J. Dahl, Short-lag spatial coherence of backscattered echoes: Imaging characteristics, IEEE Trans. Ultrason. Ferroelectr. Freq. Control 58 (7) (2011) 1377–1388.

[28] D. Hyun, A. Wiacek, S. Goudarzi, S. Rothlübbers, A. Asif, K. Eickel, Y.C. Eldar, J. Huang, M. Mischi, H. Rivaz, et al., Deep learning for ultrasound image formation: CUBDL evaluation framework and open datasets, IEEE Trans. Ultrason. Ferroelectr. Freq. Control 68 (12) (2021) 3466–3483.

[29] S. Goudarzi, H. Rivaz, Deep reconstruction of high-quality ultrasound images from raw plane-wave data: A simulation and in vivo study, Ultrasonics 125 (2022) 106778.

[30] J.-Y. Lu, P.-Y. Lee, C.-C. Huang, Improving image quality for single-angle plane wave ultrasound imaging with convolutional neural network beamformer, IEEE Trans. Ultrason. Ferroelectr. Freq. Control 69 (4) (2022) 1326–1336.

[31] A. Rodriguez-Molares, H. Torp, B. Denarie, L. Løvstakken, The angular apodization in coherent plane-wave compounding [correspondence], IEEE Trans. Ultrason. Ferroelectr. Freq. Control 62 (11) (2015) 2018–2023.

[32] A. Rodriguez-Molares, L. Lovstakken, B. Denarie, H. Torp, Busting the ghost in coherent plane-wave imaging, in: IEEE Int Ultrason Symp. Taipei, Taiwan, 2015.

[33] A. Rodriguez-Molares, J. Avdal, H. Torp, L. Løvstakken, Axial lobes in coherent plane-wave compounding, in: 2016 IEEE International Ultrasonics Symposium, IUS, IEEE, 2016, pp. 1–4.

[34] H. Embrechts, D. Roose, A parallel Euclidean distance transformation algorithm, Comput. Vis. Image Underst. 63 (1) (1996) 15–26.

[35] Y. Mishchenko, A fast algorithm for computation of discrete Euclidean distance transform in three or more dimensions on vector processing architectures, Signal Image Video Process. 9 (1) (2015) 19–27.

[36] T.E. Schouten, E.L. Van den Broek, Fast exact euclidean distance (FEED): A new class of adaptable distance transforms, IEEE Trans. Pattern Anal. Mach. Intell. 36 (11) (2014) 2159–2172.

[37] A. Rodriguez-Molares, O.M.H. Rindal, J. D'hooge, S.-E. Måsøy, A. Austeng, M.A.L. Bell, H. Torp, The generalized contrast-to-noise ratio: A formal definition for lesion detectability, IEEE Trans. Ultrason. Ferroelectr. Freq. Control 67 (4) (2019) 745–759.

[38] O.M.H. Rindal, A. Austeng, A. Fatemi, A. Rodriguez-Molares, The effect of dynamic range alterations in the estimation of contrast, IEEE Trans. Ultrason. Ferroelectr. Freq. Control 66 (7) (2019) 1198–1208.

[39] N. Bottenus, B.C. Byram, D. Hyun, Histogram matching for visual ultrasound image comparison, IEEE Trans. Ultrason. Ferroelectr. Freq. Control 68 (5) (2020) 1487–1495.

[40] A. Rodriguez-Molares, O.M.H. Rindal, O. Bernard, A. Nair, M.A.L. Bell, H. Liebgott, A. Austeng, et al., The ultrasound toolbox, in: 2017 IEEE International Ultrasonics Symposium, IUS, IEEE, 2017, pp. 1–4.

[41] H. Liebgott, A. Rodriguez-Molares, F. Cervenansky, J.A. Jensen, O. Bernard, Plane-wave imaging challenge in medical ultrasound, in: 2016 IEEE International Ultrasonics Symposium, IUS, IEEE, 2016, pp. 1–4.

[42] J.A. Jensen, Field: A program for simulating ultrasound systems, Med. Biol. Eng. Comput. 34 (sup. 1) (1997) 351–353.

[43] J.A. Jensen, N.B. Svendsen, Calculation of pressure fields from arbitrarily shaped, apodized, and excited ultrasound transducers, IEEE Trans. Ultrason. Ferroelectr. Freq. Control 39 (2) (1992) 262–267.